FUDMA Journal of Sciences (FJS)
ISSN online: 2616-1370
ISSN print: 2645 - 2944
Vol. 10 No. 23, December, 2026, pp 378 – 386
DOI: https://doi.org/10.33003/fjs-2026-1023-6557

Multiscale Structural and Microstructural Characterization of Bract Derived ZnO Relating XRD Coherent Domains to Micrometer Scale Secondary Structures

[1]Huzaifa Ali Saleh, [1]Akhilesh Dwivedi, *[1,2]Hamza Mustapha Umar, [1]Ibrahim Abba Ibrahim, [2]Maryam Ibrahim

[1]Department of Physics Mewar University Chittorgarh, India.
[2]Department of Physics, Northwest University Kano, Nigeria (Maitama Sule University Kano, Nigeria).

*Corresponding authors' email: hamzamustaphaumar@gmail.com

Received: 02 Step. 2026
Accepted: 17 Nov. 2026
Published: 18 Nov. 2026

ABSTRACT
The synthesis of zinc oxide (ZnO) with the help of plants can be dependent on the precursor chemistry, the content of the extract, and post-precipitation treatment. Complementary studies of crystal structure, diffraction-coherent domain length, secondary morphology, vibrational response, and elemental composition were used to analyze ZnO powder synthesized using an aqueous extract of red-purple *Bougainvillea spectabilis* bracts. Dried bracts (10g) were extracted with deionized water (250 mL) at 65°C for 40 min. The extract (50 mL) was added to an aqueous solution of zinc acetate dihydrate at 65°C, and the pH was adjusted to 12 with 1 M NaOH. The precipitate was aged for 60 min, dried at 80°C for 5 h and calcined at 450°C for 2 h. The XRD reflections matched hexagonal wurtzite ZnO with lattice parameters a = 3.237 Å and c = 5.186 Å. Doublet-resolved profile fitting gave Scherrer estimates for seven reflections of 8.7 to 12.3 nm (mean 10.34 nm; sample standard deviation 1.52 nm; coefficient of variation 14.7%). These are apparent coherent-domain estimates, not particle sizes. SEM revealed compact, irregular micrometer-scale secondary structures. FTIR indicated O-H/H-O-H contributions, carbonate/carboxylate-type bands, and a terminal low wavenumber absorption with an unresolved band center. EDX of one analyzed area revealed Zn and O as the main elements and carbon; its ZnO ratio is not quantitatively reliable. The results indicate that XRD coherent-domain length and SEM-visible secondary structures represent different structural scales; the available data do not establish primary-particle size, defect concentration, oxidation state, or functional performance.

Keywords: ZnO; *Bougainvillea spectabilis*; X-ray Diffraction; Scherrer Coherent Domain; Secondary Structure; FTIR

INTRODUCTION

Zinc oxide (ZnO) is an II-VI compound semiconductor with a direct band gap of 3.37 eV at ambient temperature and a large exciton binding energy of 60 meV. Its stable hexagonal wurtzite structure, together with its electrical, optical, and piezoelectric properties, makes ZnO intensively investigated for nanostructures and device-related applications (Borysiewicz, 2019; Morkoç & Özgür, 2009; Raha & Ahmaruzzaman, 2022).

Crystal structure and observable microstructure are distinct but complementary considerations for ZnO particles. X-ray diffraction (XRD) yields information on the lattice and diffraction-peak broadening, while microscopy reveals morphology at the scale of the image resolution. The measured features must be interpreted according to the whole synthesis history, as they can be modified by precursor chemistry, precipitation conditions, drying, and heat treatment.

Plant extracts introduce another component to the reaction environment during precursor conversion and material production. Previous investigations have shown that the extract concentration, reaction temperature, pH, and post-synthesis heating can influence the phase, apparent diffraction-coherent length, shape, and surface features of plant-mediated ZnO (Mutukwa et al., 2024; Osman et al., 2024). Plant-assisted precipitation is not only used for the synthesis of single-metal oxide nanoparticles, but also botanical extracts have been employed for the synthesis of multicomponent spinel metal oxides, e.g., Co–Cu–Zn nanoferrites, and their structural, optical, magnetic, and cytotoxic properties have been studied (Dwivedi et al., 2026). In precipitation routes, pH controls the zinc-containing species in solution, while temperature and precursor concentration might influence nucleation, growth, and aggregation (Mohammadi & Ghasemi, 2018; Wahab et al., 2009). In the present investigation, these elements were not modified independently, and so the final structure is understood as the result of the overall processing circumstances, rather than being assigned to the plant source alone. Previous work has also reported ZnO produced with *B. spectabilis* extract and characterized by XRD, SEM, TEM, EDS, and FTIR, with tests of 2,4-dinitrophenol removal (Nouri-Mashiran et al., 2022). The structural, optical, and photocatalytic results were published in a previous work using *Bougainvillea* flower and *Syzygium cumini* extracts (Girish et al., 2026). These investigations are pertinent in context but differ from the present in plant sources, processing routes, and application objectives. The Scherrer equation relates diffraction-peak broadening to an apparent coherent-domain length; it does not directly give the outer diameter of a particle or secondary structure (McGehee & Renault, 1972). ZnO crystalline domains can be present inside larger secondary structures; hence, XRD and SEM are complementary rather than interchangeable measurements (Dong et al., 2005).

Recent studies further indicate that the crystallinity, shape, surface chemistry, and application-related behavior of plant-mediated ZnO are dependent on the biological source and the synthesis technique (Chowdhury et al., 2026; Komalakshi et

al., 2025; Nanthakumar et al., 2025; Ogwuegbu et al., 2025; Ravi & Babu, 2025; Sekrafi et al., 2026; Senapati et al., 2025; Shukla et al., 2026; Veg et al., 2025). Two points nevertheless remain unresolved. First, plant-mediated ZnO studies frequently report a single Scherrer value as a particle size and compare it directly with SEM dimensions, although line broadening measures the coherently diffracting domain and also contains instrumental, peak-overlap, and strain contributions that are seldom separated (Holder & Schaak, 2019; Langford & Wilson, 1978). Second, the two closest *Bougainvillea* precedents differ from the present work in extract source and processing and were directed mainly toward optical or application testing (Girish et al., 2026; Nouri-Mashiran et al., 2022). To our knowledge, neither these nor other reports have examined how the diffraction-coherent scale of a powder prepared with red-purple *B. spectabilis* bract extract as the sole plant input relates to its micrometers-scale secondary structures, with the limits of each measurement made explicit. The present work advances this discussion by (i) deriving line widths from Kα-doublet-resolved profile fitting, including deconvolution of the overlapping reflections near 68° 2θ, (ii) bounding the sensitivity of the Scherrer estimates to the unmeasured instrumental contribution, and (iii) interpreting these estimates together with SEM, FTIR, and EDX evidence from the same powder. The present work therefore addresses a limited question: how the lattice, apparent diffraction-coherent domain scale, secondary morphology, vibrational features, and elemental composition of one bract-derived ZnO powder can be interpreted together without treating these measurements as equivalent quantities. The aim was to characterize ZnO generated by employing an aqueous extract of red-purple *B. spectabilis* bracts by XRD, SEM, FTIR, and EDX and to interpret the information provided by each technique. Special consideration was given to the difference between the nanometer-scale coherent length determined from the widening of XRD peaks and the bigger structures evident in SEM.

MATERIALS AND METHODS

Materials

Red-purple *B. spectabilis* bracts were dried, powdered, and used as the plant source. Zinc acetate dihydrate [$Zn(CH_3COO)_2 \cdot 2H_2O$] was used as the zinc precursor. Deionized (DI) water was used for extraction, precursor preparation, and washing, while ethanol was used during washing. A 1 M NaOH solution was used to adjust the pH (Umar, Sumaila, & Zangina, 2026).

2.2 Bract extraction

Ten grams of dried, powdered red-purple *B. spectabilis* bracts were dispersed in 250 mL of DI water and stirred at 65 °C for 40 min. After cooling, the mixture was filtered to remove insoluble plant material. The filtrate was collected in an amber bottle and stored under refrigeration until synthesis (Umar, Zangina, et al., 2026).

ZnO Synthesis

Zinc acetate dihydrate (2.19 g) was dissolved in 200 mL of deionized water and stirred at 65 °C for 35 min. The bract extract (50 mL) was then added dropwise while stirring. A 1 M NaOH solution was added dropwise until the pH reached 12, and the suspension was maintained at 65 °C for a further 60 min. The precipitate was separated and washed repeatedly with deionized water and ethanol, dried at 80 °C for 5 h, and calcined at 450 °C for 2 h. The resulting powder was gently ground and stored under dry conditions. The initial zinc acetate concentration was approximately 0.050 M; after adding 50 mL of extract, the nominal concentration was approximately 0.040 M before accounting for the added NaOH volume (Umar, Zangina & Sumaila et al., 2026)

Table 1: Experimental Conditions for B. Spectabilis Bract-Assisted Zno Preparation

Parameter	Condition
Plant material	10 g dried, powdered red-purple B. spectabilis bracts
Extraction	250 mL DI water; 65 °C; 40 min
Zn precursor	2.19 g $Zn(CH_3COO)_2 \cdot 2H_2O$ in 200 mL DI water
Precursor conditioning	65 °C; 35 min
Plant extract	50 mL
pH	1 M NaOH to pH 12
Post-addition aging	65 °C; 60 min
Washing	DI water and ethanol
Drying	80 °C; 5 h
Calcination	450 °C; 2 h

Characterization

All measurements were made on one powder obtained from a single synthesis batch; no independent synthesis replicates were prepared, and each technique was applied once to this powder. The results therefore describe this batch and do not quantify batch-to-batch variability. Powder XRD patterns were acquired using a PANalytical Empyrean diffractometer (θ–θ Bragg–Brentano geometry, Cu anode) over 2θ = 20–80° with a step size of 0.03° (2000 scan points), at a tube voltage of 45 kV and a current of 40 mA. The scan was continuous, with a counting time of 2 s per step. A fixed divergence slit of 0.38 mm and a receiving slit of 0.38 mm were used, and the specimen was mounted on a programmable xy stage with z-adjustment. The instrument record lists Cu Kα1 = 1.540598 Å and Kα2 = 1.544426 Å with a reported intensity ratio of 0.5 and indicates that no monochromator was used.

FTIR data covered 4000–400 cm^{-1} with a data interval of 1 cm^{-1} and were exported in transmittance. The spectrum in Fig. 3 is plotted directly from this export, without smoothing or baseline correction. The sampling mode, spectral resolution, number of co-added scans, and background procedure are not recorded in the exported data file available to the authors and are therefore not reported.

For SEM–EDX, the powder was Au-coated to prevent charging, as shown by the Au lines in the EDX spectra. Secondary-electron images were recorded at 15.0 kV, a working distance of 5.7 mm, and 6000× magnification (pixel size 35 nm). EDX spectra and Zn, O, and C elemental maps of the same field were acquired with a Bruker energy-dispersive X-ray system at the same accelerating voltage and working distance. The spectra were collected over the full frame of the field shown in Fig. 5a. Quantification was performed by the instrument software, which reported net

counts, unnormalized and normalized mass percentages, atomic percentages, and 3σ absolute errors for the elements selected. Au lines were identified but excluded from the normalized totals.

XRD Analysis

Interplanar spacings (d) were calculated from Bragg's law, $n\lambda = 2d \sin\theta$, using the Cu Kα1 wavelength. For hexagonal wurtzite ZnO, the lattice parameters were calculated from $a = 2d_{100}/\sqrt{3}$ and $c = 2d_{002}$. Peak positions and widths were obtained by weighted least-squares profile fitting in Python (SciPy). Each reflection was modelled as a pseudo-Voigt Kα1 component plus a Kα2 component with the same FWHM and Lorentzian fraction, half the intensity, and a position fixed by the Kα2/Kα1 wavelength ratio. The background was modelled as a straight line within each fitting window (29.5–38.8°, 45.0–50.5°, 54.0–59.5°, 60.5–65.5°, and 64.8–71.5° 2θ), and residuals were weighted by counting statistics. The (100), (002), and (101) reflections were fitted together, and the broad feature near 68° was fitted with three components assigned to (200), (112), and (201). The reported 2θ and FWHM are those of the Kα1 component. Apparent coherent-domain lengths were estimated with the Scherrer equation, $D_{app} = K\lambda/(\beta \cos\theta)$, where K = 0.9 and β is the fitted Kα1 full width at half maximum (FWHM) expressed in radians (Langford & Wilson, 1978). No instrumental reference standard (e.g., LaB_6 or Si) was measured, so instrumental broadening could not be removed directly. Its possible effect was therefore bounded by assuming an instrumental FWHM of 0.05–0.10° and applying both quadratic (Gaussian) and linear (Lorentzian) subtraction. The mean, sample standard deviation, and coefficient of variation are descriptive summaries across the seven principal reflections; they are not a particle-size distribution or a measure of replicate-to-replicate synthesis variability. Because peak width may depend on background selection, peak overlap, profile shape, and microstrain, the values should be treated as approximate apparent coherent-domain estimates.

RESULTS AND DISCUSSION

Synthesis Route and Phase Formation

The preparation comprised bract extraction, precursor conditioning, extract addition, alkaline precipitation, washing, drying, and calcination. Increasing the pH to 12 produced a zinc-containing precipitate. Subsequent drying and calcination at 450 °C yielded a crystalline powder whose principal diffraction reflections were consistent with ZnO. The final structure should therefore be interpreted as the combined result of the precursor chemistry, bract extract, alkaline precipitation, and thermal treatment.

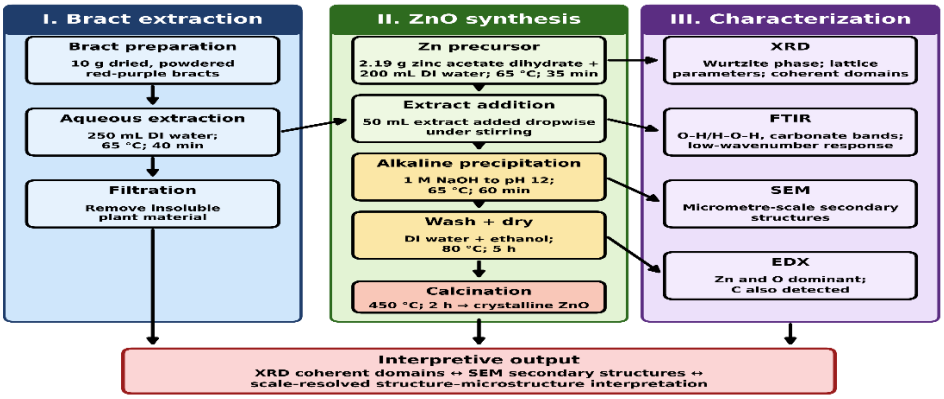


Figure 1: Experimental Workflow and Scale-Resolved Characterization of B. Spectabilis Bract-Assisted Zno

Crystal Structure and Crystallographic Parameters

Figure 2a shows the powder diffraction pattern, replotted directly from the raw diffractometer export. The principal reflections occur at 31.90°, 34.56°, 36.36°, 47.67°, 56.72°, 63.00°, and 68.08° in 2θ (fitted Kα1 positions). They are indexed as the (100), (002), (101), (102), (110), (103), and (112) planes, respectively, of hexagonal wurtzite ZnO. The sequence is consistent with the expected wurtzite structure. No additional major crystalline phase is evident among the dominant reflections over the measured range. The weak reflections near 72.6° and 77.0° are consistent with the (004) and (202) planes of wurtzite ZnO, whereas the broad, low-intensity hump between about 20° and 25° remains unassigned because the available pattern does not provide sufficient evidence for its origin.

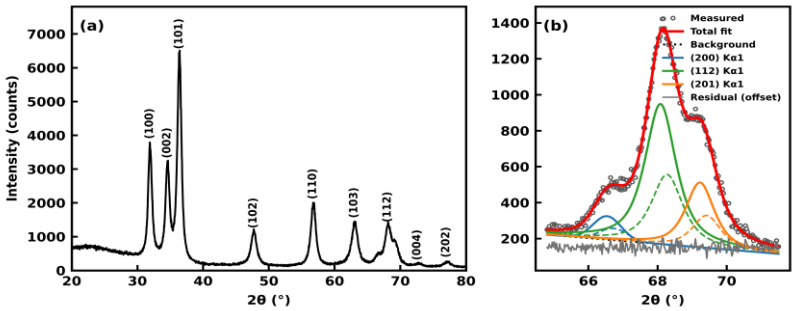


Figure 2: (A) Powder XRD Pattern of the *B. Spectabilis* Bract-Assisted Zno Sample; (B) Profile Fit of The 64.8–71.5° Region Showing The (200), (112), And (201) Components (Solid Lines, Kα1; Dashed Lines, Kα2), The Linear Background, And The Residual

The calculated d-spacings range from 2.803 Å for the (100) reflection to 1.376 Å for the (112) reflection. The (100) and (002) reflections give lattice parameters of a = 3.237 Å and c = 5.186 Å, respectively. These values are close to commonly reported room-temperature parameters for wurtzite ZnO. The small differences are not interpreted as evidence of a definite strain state because full-profile refinement and independent instrumental calibration were not performed. The apparent coherent-domain estimates derived from the fitted FWHM values are summarized in Table 2.

Fig. 2b shows that the broad feature near 68° is not a single reflection. It is reproduced by three components at 66.54°, 68.08°, and 69.23°, consistent with the (200), (112), and (201) reflections of wurtzite ZnO. If this envelope is treated as a single (112) peak, its apparent width (1.71°) includes the neighboring reflections and gives an apparent domain length of only 5.6 nm; the deconvolved (112) width is 1.074°, corresponding to 8.9 nm. With doublet-resolved fitting, the seven principal reflections give apparent domain lengths of 8.7–12.3 nm (mean 10.34 nm; sample standard deviation 1.52 nm; coefficient of variation 14.7%). Allowing for an instrumental FWHM of up to 0.10° changes these values by at most about 1% with quadratic subtraction and increases them by at most about 17% with linear subtraction (Table 2). The coherent-domain scale is therefore of the order of 10 nm under all of these assumptions.

Table 2: Profile-Fitted XRD Reflections, Kα1 FWHM Values, And Apparent Scherrer Coherent-Domain Estimates

2θ (°)	(hkl)	d (Å)	FWHM (°)	D_{app} (nm)	D_{app}, β_{inst} = 0.10° (nm)
31.898	(100)	2.803	0.674	12.3	12.4–14.4
34.560	(002)	2.593	0.708	11.8	11.9–13.7
36.359	(101)	2.469	0.723	11.6	11.7–13.4
47.674	(102)	1.906	0.981	8.9	8.9–9.9
56.720	(110)	1.622	0.878	10.3	10.3–11.6
62.998	(103)	1.474	1.066	8.7	8.8–9.6
66.541	(200)	1.404	0.948	10.0	10.1–11.2
68.084	(112)	1.376	1.074	8.9	9.0–9.8
69.227	(201)	1.356	0.980	9.8	9.9–11.0
Mean ± SD (7 principal)				10.34 ± 1.52	

Note: 2θ and FWHM refer to the Kα1 component of doublet-resolved pseudo-Voigt fits. D_{app} is the uncorrected apparent coherent-domain length. The last column gives the range obtained by quadratic and linear subtraction of an assumed instrumental FWHM of 0.10°. The (200) and (201) components were resolved within the 68° envelope and are not included in the summary statistics. The values should not be interpreted as primary-particle diameters or as evidence of a particle-size distribution.

FTIR Response and Surface-Associated Features

The FTIR spectrum is shown in Fig. 3. A broad feature near 3393 cm^{-1} and a weak feature around 1642 cm^{-1} are consistent with O–H stretching and H–O–H bending, respectively, and may reflect surface hydroxyl groups and/or adsorbed moisture. The band at 1381 cm^{-1}, together with the weaker shoulder near 1500 cm^{-1}, falls in the range of the symmetric and asymmetric O–C–O stretching vibrations of carboxylate or carbonate groups (Nakamoto, 2009). These may arise from residual acetate-derived species or from surface carbonate formed by adsorption of atmospheric CO_2 on ZnO; the present data do not distinguish between these sources. The weak feature near 878 cm^{-1} is consistent with the out-of-plane bending (ν_2) mode of carbonate and supports a carbonate contribution (Nakamoto, 2009). The broader band at 995 cm^{-1}, with a shoulder near 1100 cm^{-1}, lies in the region of C–O stretching in oxygenated organic species and may indicate a small carbonaceous residue that survived calcination, which would be consistent with the carbon detected by EDX (Section 3.4). The weak features at 746, 689, and 627 cm^{-1} lie just above the strong low-wavenumber absorption edge. They may involve carbonate in-plane bending (ν_4) or the high-frequency side of the Zn–O lattice absorption, but they are too weak and overlapping to be assigned individually. The small feature near 2320–2360 cm^{-1} is attributed to incompletely compensated atmospheric CO_2. Specific plant-derived molecules are not assigned because the bract extract was not characterized independently.

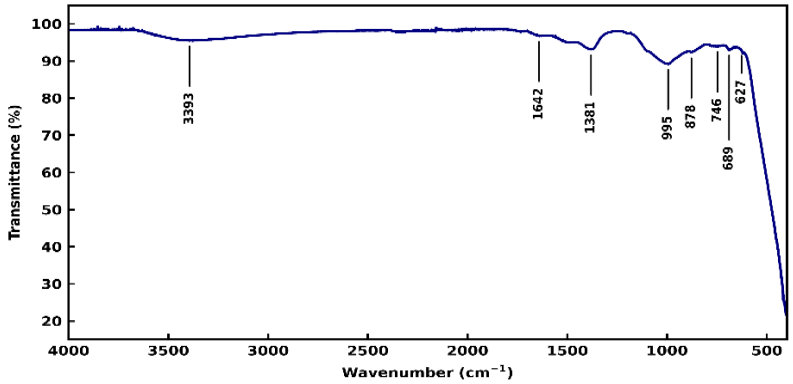


Fig 3: FTIR Spectrum of the Calcined *B. spectabilis* Bract-assisted ZnO Sample, Replotted from the Raw Transmittance Export with Band Positions Marked

The raw FTIR export shows transmittance decreasing from 58.11% at 500 cm^{-1} to 21.22% at 400 cm^{-1}. This downturn corresponds to increasing apparent absorption toward the low-wavenumber boundary, but no local absorption-band center is resolved before the measurement limit. The terminal response may include Zn–O-related lattice absorption; however, it is not independently diagnostic, and the phase assignment rests primarily on XRD.

Morphology, Secondary Structure, and Elemental Composition

The SEM micrograph in Fig. 4 shows compact, irregular secondary structures several micrometers across, together with smaller clustered fragments. In this work, the term secondary structure is used descriptively for these micrometers-scale assemblies. The terms aggregate and agglomerate are avoided because they imply a bonding strength between the constituent units, which was not measured (Nichols et al., 2002). Fine surface texture is visible, but the available magnification does not resolve the primary crystalline domains sufficiently for reliable sizing. A primary-particle size distribution was therefore not extracted from this image. Only one field of view was recorded at 6000× during the available instrument session. This field is therefore used for a qualitative description of the analyzed area only; it is not used to infer a size distribution of the secondary structures or the arrangement of the nanometer-scale domains. The Zn, O, and C maps of the same field (Fig. 6) provide additional views of this area.

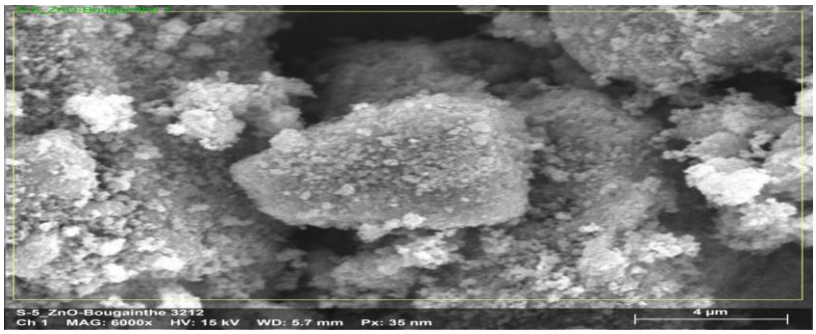


Figure 4: SEM Secondary-Electron Image at 6000x, 15.0 Kv, Working Distance 5.7 Mm, With A 4 µm Scale Bar

Fig. 5 shows the analysed area and the EDX spectra. Both spectra were acquired over the full frame of the field in Fig. 5a and therefore describe the same location rather than two separate regions. They differ in the element list used for quantification: quantification 1 included C, O, and Zn (Fig. 5b), whereas quantification 2 included O and Zn only (Fig. 5c). The exported values were checked against the software report, which confirms that the percentages used here are normalized atomic percentages; the corresponding mass percentages, 3σ errors, and unnormalized totals are listed in Table 3. Zinc and oxygen are the principal detected elements. Carbon may originate from the sample mount, a carbonaceous residue, or surface carbonate (Section 3.3). The Au peaks are associated with the conductive coating used for SEM–EDX analysis.

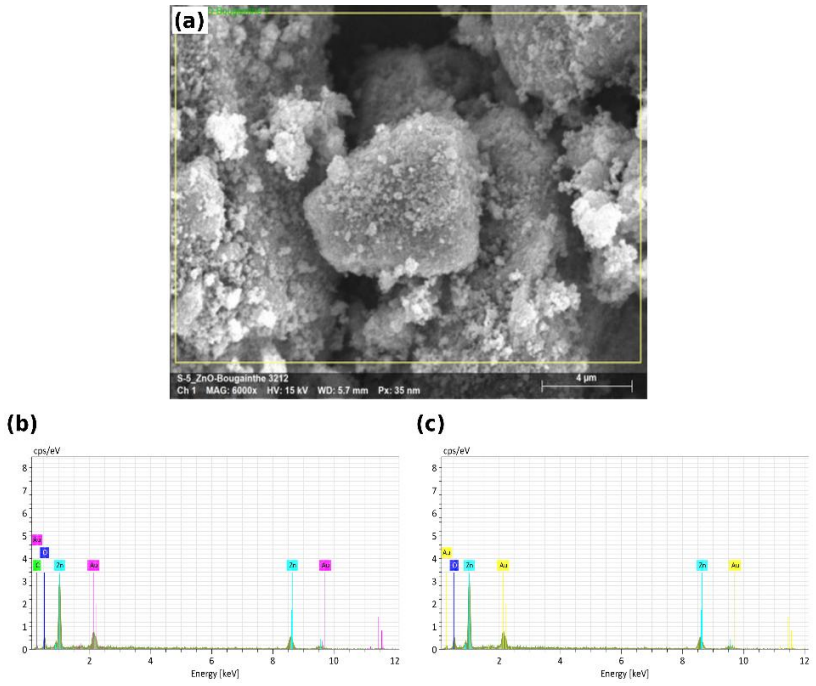


Fig 5: (a) SEM field analyzed by EDX, with the full-frame acquisition area marked by the yellow frame; (b) EDX spectrum quantified with C, O, and Zn; (c) EDX spectrum quantified with O and Zn. Au is associated with the conductive coating

Table 3: EDX Quantification of the Same Full-Frame Area with Two Element Lists, Compared with Stoichiometric Zno

Quantification	Element	Mass % (normalized)	Atomic %	3σ abs. error (wt.%)	Unnormalized total (wt.%)
1 (C, O, Zn)	C	4.42	17.22	1.41	23.35
	O	6.48	18.96	1.22	
	Zn	89.11	63.82	2.63	
2 (O, Zn)	O	6.44	21.95	1.04	22.49
	Zn	93.56	78.05	2.49	
Stoichiometric ZnO	O	19.66	50.00	–	–
	Zn	80.34	50.00	–	–

These percentages cannot be read as a Zn:O stoichiometry. The atomic Zn:O ratios are 3.37 (quantification 1) and 3.56 (quantification 2), whereas ZnO requires 1:1. In mass terms, the normalized O content is about 6.5 wt.%, compared with 19.7 wt.% for stoichiometric ZnO, so oxygen is under-recovered by a factor of about three. The unnormalized analytical totals were only 23.35 and 22.49 wt.%, far below the value near 100% expected for a reliable analysis, which shows that the raw X-ray intensities were strongly affected by the measurement conditions. Likely causes are absorption of the low-energy O Kα line (0.525 keV) in the rough, porous powder and in the Au coating, shadowing of the detector by surface topography, and the quantification of a rough, non-flat specimen whose geometry departs from the flat, polished sample the correction model assumes (Goldstein et al., 2018). Normalizing such low totals to 100% amplifies these errors. Omitting Au from the normalization does not explain the imbalance; the dominant factor is the under-recovery of oxygen. Consistent with this, the elemental maps (Fig. 6) show Zn signal across the whole field, whereas the O and C signals are weaker in recessed, shadowed areas, as expected for strongly absorbed low-energy X-rays rather than for genuine compositional differences. The EDX results are therefore used only qualitatively, to confirm that Zn and O are the principal elements and that C is present. They are not taken as evidence of oxygen deficiency or of any defect chemistry.

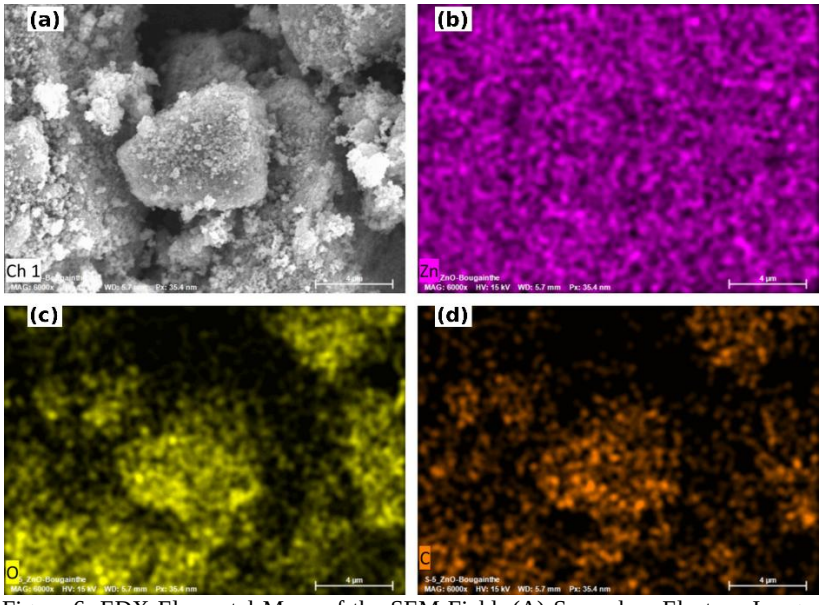


Figure 6: EDX Elemental Maps of the SEM Field: (A) Secondary-Electron Image, (B) Zn, (C) O, And (D) C (15.0 Kv, 6000×, Scale Bars 4 µm)

Discussion

Integrated Interpretation of Structure and Microstructure

The methods provide complementary information about the same powder at different structural levels. XRD is consistent with the wurtzite ZnO lattice and provides apparent coherent-domain estimates. SEM reveals larger micrometers-scale secondary structures. FTIR shows features consistent with surface-associated hydroxyl/water contributions, carbonate/carboxylate-type species, and a terminal low-wavenumber absorption response whose band center is unresolved; EDX identifies Zn and O as the principal detected elements. The apparent Scherrer estimates range from 8.7 to 12.3 nm, whereas SEM resolves secondary structures on the micrometers scale. These observations are compatible with small diffraction-coherent domains occurring within larger secondary structures, but the available SEM image does not directly resolve or prove the arrangement of the primary domains. The two measurements quantify different features: XRD broadening reflects diffraction coherence, while SEM records the morphology visible at the selected magnification. 4.2 Comparison with previous Bougainvillea-mediated ZnO studies

Table 4 compares the present dataset with two closely related studies of *Bougainvillea*-mediated ZnO. The earlier *B. spectabilis* study used TEM in addition to XRD, SEM, EDS, and FTIR and included application testing. The more recent flower-based study included optical and photocatalytic measurements. The present work instead focuses on the structural, microstructural, vibrational, and elemental evidence available for the bract-derived powder.

Table 4: Comparison with Representative Bougainvillea-Mediated Zno Studies

Study	Biological source	Main measurements / application	Relation to present study
Nouri-Mashiran et al. (2022)	B. spectabilis extract	XRD, SEM, TEM, EDS, FTIR; 2,4-dinitrophenol removal	Direct B. spectabilis precedent; includes TEM and application testing not used here
Girish et al. (2026)	Bougainvillea flower extract with Syzygium cumini	XRD, diffuse reflectance, SEM; UV photocatalysis	Recent flower-based study; biological source and optical/application dataset differ
Present study	Red-purple B. spectabilis bracts	XRD, FTIR, SEM-EDX	Focus on lattice parameters, coherent domains, secondary structures, vibrational response, and elemental composition

The main contribution of the present dataset is its side-by-side interpretation of several length scales measured for one bract-derived ZnO powder. The available data do not establish primary-particle diameter, defect chemistry, oxidation state, optical band structure, or photocatalytic performance; these properties are not assigned here.

Relating Processing History to the Measured Length Scales

The processing history and the structural scales examined in this study are summarized in Fig. 1. The bract extract forms part of the reaction environment; alkaline treatment produces the precipitated precursor; and drying followed by calcination yields the crystalline powder. XRD describes the lattice and apparent coherent-domain scale, SEM reveals larger secondary morphology, and FTIR and EDX provide complementary vibrational and elemental information. The links in Fig. 1 represent a proposed relation between processing history and ex-situ measurements rather than direct observations during synthesis.

A coherent-domain length estimated from diffraction-peak broadening describes the scale over which lattice planes contribute coherently to the diffraction signal. It is not, by itself, the external diameter of a particle or secondary structure. The combination of broadened XRD peaks and micrometers-scale SEM secondary structures is compatible with a hierarchical powder structure, but the present measurements do not resolve the primary-particle population or directly establish how the domains are assembled.

Limitations and Implications

The present characterization supports the wurtzite ZnO phase assignment and describes morphology, vibrational features, and elemental composition. It does not support quantitative claims about primary-particle size, defect concentration, or oxidation state. The primary domains are not resolved in the SEM image, instrumental contributions to XRD peak broadening were bounded but not measured with a reference standard, the FTIR data do not identify individual plant metabolites, and EDX remains semi-quantitative, with oxygen strongly under-recovered. Only one synthesis batch and one SEM field were examined. More detailed work could include transmission electron microscopy (TEM) or high-resolution TEM to examine primary morphology, photoluminescence spectroscopy to probe defect-related optical emission (Özgür et al., 2005; Vanheusden et al., 1996), and X-ray photoelectron spectroscopy (XPS) to investigate surface chemical states (Chen et al., 2000). These additional measurements would test questions not resolved by the present dataset.

CONCLUSION

The XRD pattern is in good agreement with hexagonal wurtzite ZnO (a = 3.237 Å and c = 5.186 Å). The uncorrected Scherrer estimates from doublet-resolved profile fitting are in the range of 8.7 nm to 12.3 nm with a mean of 10.34 nm, a sample SD of 1.52 nm, and a coefficient of variation of 14.7%; the broad feature near 68° contains the (200), (112), and (201) reflections, and a plausible instrumental contribution changes the estimates by no more than about 17%. In SEM, compact, irregular micrometers-scale secondary structures can be seen. FTIR features are consistent with the surface-associated hydroxyl/adsorbed-water contribution and carbonate/carboxylate-type species; there is a low wavenumber absorption response, but it is unresolved, and the band center is not independently diagnostic for Zn–O. EDX confirms that the primary elements identified are Zn and O, with carbon detected when included in the quantification; the measured Zn:O ratio is unreliable because oxygen was strongly under-recovered. The results, when combined, show that the apparent diffraction coherent length was different from the larger-scale morphology observed in the SEM. The characterization is confined to the properties deduced from the measurements and is not a determination of primary-particle diameter, defect chemistry, optical properties, or photocatalytic activity.

REFERENCES

Borysiewicz, M. A. (2019). ZnO as a functional material, a review. *Crystals*, *9*(10), 505. https://doi.org/10.3390/cryst9100505

Chen, M., Wang, X., Yu, Y. H., Pei, Z. L., Bai, X. D., Sun, C., Huang, R. F., & Wen, L. S. (2000). X-ray photoelectron spectroscopy and auger electron spectroscopy studies of Al-doped ZnO films. *Applied Surface Science*, *158*(1–2), 134–140. https://doi.org/10.1016/S0169-4332(99)00601-7

Chowdhury, N. R., Pritha, N., Sajid, S., Mesbah, M. B., Islam, M. E., Hakim, M., Mobarak, M. B., & Chowdhury, F. (2026). Plant-mediated green synthesis of ZnO nanoparticles utilizing *Garcinia cowa* leaf extract: Structural, bioactive, and in silico molecular docking insights. *Next Materials*, *10*, 101575. https://doi.org/10.1016/j.nxmate.2025.101575

Dwivedi, A., Umar, H. M., Ahmed, G., Vaswani, J., & Aamir, M. (2026). Moringa oleifera leaf extract-assisted precipitation synthesis of Co–Cu–Zn spinel nanoferrites: Structural, optical, magnetic, and cytotoxic evaluation. Journal of Alloys and Compounds Communications, Article 100300. https://doi.org/10.1016/j.jacomc.2026.100300

Dong, L., Liu, Y. C., Tong, Y. H., Xiao, Z. Y., Zhang, J. Y., Lu, Y. M., Shen, D. Z., & Fan, X. W. (2005). Preparation of ZnO colloids by aggregation of the nanocrystal subunits. *Journal of Colloid and Interface Science, 283*, 380–384. https://doi.org/10.1016/j.jcis.2004.09.044

Girish, K. M., Lavanya, R., Surendra, B. S., Gurushantha, K., Sharada, T., & Prashantha, S. C. (2026). Eco-friendly synthesis of ZnO nanoparticles using *Bougainvillea* and *Syzygium cumini* extracts: Structural, optical, and photocatalytic insights. *ChemistrySelect, 11*, e73427. https://doi.org/10.1002/slct.73427

Goldstein, J. I., Newbury, D. E., Michael, J. R., Ritchie, N. W. M., Scott, J. H. J., & Joy, D. C. (2018). *Scanning electron microscopy and X-ray microanalysis* (4th ed.). Springer. https://doi.org/10.1007/978-1-4939-6676-9

Holder, C. F., & Schaak, R. E. (2019). Tutorial on powder X-ray diffraction for characterizing nanoscale materials. *ACS Nano, 13*(7), 7359–7365. https://doi.org/10.1021/acsnano.9b05157

Komalakshi, K. V., Kamble, A. A., Barretto, D. A., Divakar, M. S., & Chalannavar, R. K. (2025). Plant-mediated ZnO nanoparticles using *Allophylus concanicus*: Synthesis, characterization, and in vitro biological evaluation. *Nano-Structures & Nano-Objects, 43*, 101524. https://doi.org/10.1016/j.nanoso.2025.101524

Langford, J. I., & Wilson, A. J. C. (1978). Scherrer after sixty years: A survey and some new results in the determination of crystallite size. *Journal of Applied Crystallography, 11*(2), 102–113. https://doi.org/10.1107/S0021889878012844

McGehee, R., & Renault, J. (1972). The use of standard deviation of X-ray diffraction lines as a measure of broadening in the Scherrer equation: A curve fitting method. *Journal of Applied Crystallography, 5*, 365–370. https://doi.org/10.1107/S002188987200977X

Mohammadi, F. M., & Ghasemi, N. (2018). Influence of temperature and concentration on biosynthesis and characterization of zinc oxide nanoparticles using cherry extract. *Journal of Nanostructure in Chemistry, 8*, 93–102. https://doi.org/10.1007/s40097-018-0257-6

Morkoç, H., & Özgür, Ü. (2009). *Zinc oxide: Fundamentals, materials and device technology*. Wiley-VCH. https://doi.org/10.1002/9783527623945

Mutukwa, D., Taziwa, R. T., & Khotseng, L. (2024). A review of plant-mediated ZnO nanoparticles for photodegradation and antibacterial applications. *Nanomaterials, 14*(14), 1182. https://doi.org/10.3390/nano14141182

Nakamoto, K. (2009). *Infrared and Raman spectra of inorganic and coordination compounds, Part A: Theory and applications in inorganic chemistry* (6th ed.). Wiley. https://doi.org/10.1002/9780470405840

Nanthakumar, J., Palanisamy, Y., Palanisamy, S., Karuppusamy, M., Raja, R., Abbas, M., Alagarsamy, A., & Rahman, M. Z. (2025). Eco-friendly synthesis of ZnO nanoparticles using *Delonix elata* extract with enhanced antibacterial activity. *RSC Advances, 15*, 39305–39313. https://doi.org/10.1039/D5RA05208D

Nichols, G., Byard, S., Bloxham, M. J., Botterill, J., Dawson, N. J., Dennis, A., Diart, V., North, N. C., & Sherwood, J. D. (2002). A review of the terms agglomerate and aggregate with a recommendation for nomenclature used in powder and particle characterization. *Journal of Pharmaceutical Sciences, 91*(10), 2103–2109. https://doi.org/10.1002/jps.10191

Nouri-Mashiran, M., Taghavi, L., Fataei, E., Ebrahimzadeh-Rajaei, G., & Ramezani, M. (2022). Green synthesis of ZnO nanoparticles and comparison of 2,4-dinitrophenol removal efficiency using photocatalytic, sonocatalytic, and adsorption processes. *Main Group Chemistry, 21*, 559–575. https://doi.org/10.3233/MGC-210152

Ogwuegbu, M. C., Olatunde, O. C., Pfukwa, T. M., Mthiyane, D. M. N., Fawole, O. A., & Onwudiwe, D. C. (2025). Green synthesis, characterization and antimicrobial activity of ZnO and Co-doped ZnO nanoparticles obtained using aqueous extracts of *Platycladus orientalis* leaves. *Discover Materials, 5*(1), 55. https://doi.org/10.1007/s43939-025-00230-w

Osman, A. I., Zhang, Y., Farghali, M., Rashwan, A. K., Eltaweil, A. S., Abd El-Monaem, E. M., Mohamed, I. M. A., Badr, M. M., Ihara, I., Rooney, D. W., & Yap, P.-S. (2024). Synthesis of green nanoparticles for energy, biomedical, environmental, agricultural, and food applications: A review. *Environmental Chemistry Letters, 22*(2), 841–887. https://doi.org/10.1007/s10311-023-01682-3

Özgür, Ü., Alivov, Y. I., Liu, C., Teke, A., Reshchikov, M. A., Doğan, S., Avrutin, V., Cho, S.-J., & Morkoç, H. (2005). A comprehensive review of ZnO materials and devices. *Journal of Applied Physics, 98*(4), 041301. https://doi.org/10.1063/1.1992666

Raha, S., & Ahmaruzzaman, M. (2022). ZnO nanostructured materials and their potential applications: Progress, challenges and perspectives. *Nanoscale Advances, 4*, 1868–1925. https://doi.org/10.1039/D1NA00880C

Ravi, P., & Babu, S. (2025). Recent development in plant-mediated zinc oxide nanoparticles with biomedical applications. *Chemical Physics Impact, 10*, 100870. https://doi.org/10.1016/j.chphi.2025.100870

Sekrafi, T., Echabaane, M., Ly, A., Debliquy, M., Dridi, C., & Lahem, D. (2026). Green synthesis of ZnO nanoparticles using *Retama raetam* leaf extract for VOC sensing applications. *Chemosensors, 14*(2), 42. https://doi.org/10.3390/chemosensors14020042

Senapati, U. S., Chauhan, P., Kalita, H., Das, A., Saikia, J., Goswami, M., Deka, H., & Barman, T. (2025). Green synthesis, characterization and bioactivity of zinc oxide nanoparticles: Experimental and computational approaches. *Next Nanotechnology, 7*, 100194. https://doi.org/10.1016/j.nxnano.2025.100194

Shukla, M., Narain, S., Kumar, A., & Dikshit, A. (2026). Zinc oxide nanoparticles: A plant-mediated synthesis, characterizations and their functional applications. *Nano Trends, 13*, 100184. https://doi.org/10.1016/j.nwnano.2026.100184

Umar, H. M., Sumaila, J. L., & Zangina, T. (2026). Comparative structural, optical, morphological and elemental characterization of jujube-mediated silver and zinc oxide nanoparticles. *FUDMA Journal of Sciences*, *10*(19), 219–229. https://doi.org/10.33003/fjs-2026-1019-6073

Umar, H. M., Zangina, T., Sumaila, J. L., Vasamsetti, T., & Dwivedi, A. (2026). From *Ziziphus jujuba* leaves to nanoparticles: Green synthesis and characterization of Ag and ZnO nanostructures. *International Journal of Scientific Research and Technology*, *3*(10), 695–704. https://doi.org/10.5281/zenodo.23279649

Umar, H. M., Zangina, T., Sumaila, J. L., Dwivedi, A., & Aamir, M. (2026). Green synthesis of silver and zinc oxide nanoparticles using Ziziphus jujuba: Mechanisms, characterization, applications, and future perspectives. Journal of Materials Science: Materials in Energy, 2, 9. https://doi.org/10.1007/s44308-026-00021-6

Vanheusden, K., Warren, W. L., Seager, C. H., Tallant, D. R., Voigt, J. A., & Gnade, B. E. (1996). Mechanisms behind green photoluminescence in ZnO phosphor powders. *Journal of Applied Physics*, *79*(10), 7983–7990. https://doi.org/10.1063/1.362349

Veg, E., Raza, A., Rai, S., Bansal, P., Sharma, S., Mishra, N., Gupta, R., Mishra, S., Joshi, S., Khan, A. R., & Khan, T. (2025). Green synthesis of ZnO and α-Fe_2O_3 nanoparticles using Chinese fan palm leaf extract for their biological and photocatalytic activity evaluation. *RSC Sustainability*, *3*, 5609–5631. https://doi.org/10.1039/D5SU00349K

Wahab, R., Kim, Y.-S., & Shin, H.-S. (2009). Synthesis, characterization and effect of pH variation on zinc oxide nanostructures. *Materials Transactions*, *50*, 2092–2097. https://doi.org/10.2320/matertrans.M2009099

©2026 This is an Open Access article distributed under the terms of the Creative Commons Attribution 4.0 International license viewed via https://creativecommons.org/licenses/by/4.0/ which permits unrestricted use, distribution, and reproduction in any medium, provided the original work is cited appropriately.